# Relaxation dynamics of a flexible rod in a fluid

Ayrton Draux [ORCID],[1] Hoa-Ai Béatrice Hua,[2] Pascal Damman [ORCID],[1] and Fabian Brau [ORCID][2,*]

[1]*Laboratoire Interfaces & Fluides Complexes, Université de Mons, 20 Place du Parc, B-7000 Mons, Belgium*
[2]*Université libre de Bruxelles (ULB), Nonlinear Physical Chemistry Unit, CP231, 1050 Bruxelles, Belgium*

The relaxation dynamics of a bent rod immersed in a fluid is studied experimentally for various rod materials and sizes and fluid viscosities. One extremity of the rod is clamped while its free end is displaced from its equilibrium position by a controlled distance. For large bending stiffness or low viscosity, the dynamics is underdamped and the rod oscillates around its equilibrium position with a well-defined frequency and a damped amplitude. In contrast, for low bending stiffness or large viscosity, the dynamics is overdamped and the rod relaxes to its equilibrium position without oscillating. We show the existence of two overdamped regimes where the relaxation dynamics is characterized by two different polynomial decays showing that the viscous force is not proportional to the rod velocity. The system is modeled using the dynamical beam equation supplemented by the viscous force experienced by a rigid cylinder moving at a constant speed in a fluid. In spite of this approximation, the model describes the dynamics in good approximation and provides a simple explanation for the existence of two overdamped regimes which originate from a change of the viscous force behavior as the Reynolds number varies. The model is then used to characterize the overdamped relaxation dynamics of the papillae of the bee tongues observed during nectar feeding. We show that the papillae relaxation is not complete when the sugar concentration exceeds 30% which impacts the amount of nectar collected per lap and yields an optimal concentration around 55% for the energy intake rate.

## I. INTRODUCTION

As shown in countless studies, the deflection and vibration of slender structures have found applications in various aspects of nanotechnology, their most widespread use being probably the design of cantilevers in atomic force microscopy [1,2]. The high sensitivity of the resonance frequency of oscillating thin plates or rods to minute modifications of their structure allows the design of new generations of devices used for chemical detection [3–7], photothermal spectroscopy [8], biological sensors and assays [9–13], or for measuring various physical quantities such as density or viscosity [14] to name a few (for a recent review, see [15]). In some cases, these devices operate in a viscous environment and an accurate description of the fluid-structure coupling is necessary to optimize the sensing capabilities of these nanosensors and microsensors. In all these studies, the theoretical models typically assume that the amplitude of vibration of the beam is far smaller than any length scale in the beam geometry and approximate the hydrodynamic force acting along the deforming elastic beam by the one given by the two-dimensional flow generated by a corresponding rigid cylinder of identical cross section and oscillation amplitude [16–21]. This approximation has been validated by both numerical simulations of the full three-dimensional flow and experiments [18,22].

---

*fabian.brau@ulb.be

The periodic motion of a thin flexible structure in a fluid arises also in a large number of biophysical problems. For example, the locomotion of some micro-organisms, such as spermatozoa or flagellar bacteria, has been studied by considering the periodic forcing of a flexible flagellum confined in a plane to estimate the fluid forces and the swimming speed [23–30]. The nonplanar motion of flagella observed in the locomotion of many micro-organisms has been described through rotating elastica. As the applied torque increases the profile of the filament changes from gently bent to a helical shape leading to a significant increase of the propulsive force [31–34]. The rotation of helical flexible filaments has also been studied to determine under which conditions a propulsion is possible since this structure may experience a buckling instability [35–40]. The main challenge in modeling these fluid-structure interaction problems arises from the need to couple the structural mechanics of the flagellum with an accurate description of the hydrodynamic loading induced by the fluid. This coupling is generally achieved by using the resistive force theory which neglects hydrodynamic interactions between flows induced by different parts of the elastic beam [26,28] or the Stokeslet and slender body theories which both rely on the linearity of the Stokes equations for flows at low Reynolds numbers [28,41,42].

In all these aforementioned cases, the slender structure is forced through a periodic motion either to reach a resonance frequency in sensor devices or to induce a propulsion for the locomotion of micro-organisms. The relaxation dynamics of a bent flexible filament immersed in a fluid has received less attention whereas the relaxation of a filament at a fluid interface has been recently studied [43]. Such a system could, however, meet applications in biology. Indeed, bats, hummingbirds, and some insects feed by dipping periodically in the flower nectar their tongue decorated with flexible microstructures [44–50]. For instance, the drinking cycle of bees involves the periodic protraction and retraction of their tongue covered by elongated papillae forming a hairy structure. During the tongue protraction, the hairy structure, initially adhering to the tongue (glossa) by capillary forces [51,52], relaxes to a widely open brushlike shape when immersed in the nectar. During the retraction, this peculiar tongue's morphology allows the nectar to be trapped by viscous entrainment and capillary forces and finally driven to the bee's mouth [53–63]. The amount of nectar collected per laps is essentially constant at sufficiently low sugar concentration but drops sharply when the sugar content exceeds around 60% [62–65]. Very recently, the loss of efficiency of the bees' tongue in capturing very sweet nectar has been related to the relaxation dynamics of their slender papillae which can be modeled as flexible rods [63].

The aim of this paper is to study the full spectra of relaxation dynamics observed for bent flexible rods in a fluid with a special emphasis on the overdamped regime. We consider clamped rods slightly deflected at their free end. In Sec. II, we report a series of experiments conducted with rods of various dimensions made of contrasted materials immersed in liquids of drastically different viscosity. The results of these experiments have been reported elsewhere [63] but only one of the three identified regimes has been briefly discussed. The goal of this paper is to provide a detailed description of the dynamics for all observed regimes. For the theoretical analysis presented in Sec. III, we propose a simplified model obtained by decoupling the fluid equations from the rod elasticity and assuming an effective drag force for the rod geometry. The asymptotic analyses for the overdamped and underdamped regimes are derived and quantitatively compared to experimental results in Sec. IV. In spite of its simplifying assumptions, the model shows an impressive quantitative agreement with the experimental data and provides a new insight into this intricate problem. The application of the model to the bee's papillae relaxation dynamics is described in Sec. VI. We show that the papillae are not fully erected when the sugar concentration exceeds roughly 30%.

## II. EXPERIMENTS AND RESULTS

The experiments described in this section have been briefly presented in Ref. [63] with an emphasis on the overdamped regime relevant for dynamics of bee's papillae. We recall the experimental setup here for completeness and discuss in more detail the results and in particular the raw data and associated scalings for all regimes.

### A. Experimental methods

We consider rods of length $L$, radius $R$, Young modulus $E$, and density $\rho_s$ clamped at one extremity and immersed in a liquid of viscosity $\mu$ and density $\rho_l$. To cover a broad range of parameters, we used various materials for the rod, from stainless steel surgery needle to polypropylene (PP) and polylactic acid (PLA) filaments extruded from a three-dimensional (3D) printer nozzle (5 GPa $\leqslant E \leqslant$ 165 GPa). The bending and Young moduli have been determined from the profile of rods bent by a known force applied at their free end. We also considered contrasted rod geometries (1.1 cm $\leqslant L \leqslant$ 9.0 cm, 0.15 mm $\leqslant R \leqslant$ 0.4 mm). For the immersing fluid, water, glycerol, and silicone oils with viscosities ranging from $10^{-3}$ to 10 Pa s were used. The size of the fluid container ($32 \times 115 \times 60$ mm$^3$) is much larger than the rod dimension to avoid finite-size effects. The densities of both solids and liquids have been obtained by weighing a known volume of materials (1400 kg/m$^3$ $\leqslant \rho_s \leqslant$ 8300 kg/m$^3$, 950 kg/m$^3$ $\leqslant \rho_l \leqslant$ 1100 kg/m$^3$).

For all experiments, the rod is bent by manually displacing its free end with a graduated tool by a distance 0.7 mm $\leqslant d \leqslant$ 4.9 mm depending on the rod length and radius. The initial displacement of the rod tip is small with respect to rod length $d/L \ll 1$, and large with respect to the rod radius $d/R \gg 1$. Once the free end is released, the motion of the rod is recorded by a Photron Fastcam SA3 high-speed camera operating at $10^3$–$10^4$ frames per second until the rod returns to its horizontal equilibrium position. For each system, i.e., given fluid, rod, and initial displacement, the dynamics were averaged over three repetitions of the same experiment. The relaxation dynamics always occur in the plane of the bent rod since recording its motion from different angles does not reveal any lateral deviation of the rod.

Figure 1(a) shows few snapshots of the rod profile during its motion. Conventional image analysis yields the position of the moving tip as a function of time. Figure 1(b) shows three examples of underdamped, critically damped, and overdamped dynamics. For comparison with the theoretical model, we determine the time $T$ at which the tip of the rod crosses the horizontal axis for the first time (crossing time) and, when several oscillations are observed, the damping time $T^\star$ characterizing the decay of the oscillations' envelope.

### B. Results

The relaxation dynamics of a bent rod immersed in a fluid depends strongly on the fluid viscosity as well as on the rod materials and geometry. Indeed, for the same steel rod, Fig. 1(b) shows that, at low viscosity $\mu = 10^{-3}$ Pa s, the tip of the rod follows an underdamped motion with several oscillations before reaching its equilibrium position whereas no oscillations are observed at a higher viscosity, $\mu = 5.5$ Pa s, where the motion is completely damped. Therefore, we define the overdamped, critically damped, and underdamped regimes as the regimes where the profile $w_E(t)$ has 1, 2, or more than 2 zeros, respectively.

The motion of the rod tip in the overdamped regime, shown in Fig. 1(c), reveals a striking feature of the relaxation dynamics. For a classical overdamped oscillator with a damping term proportional to the velocity, the system returns to equilibrium without oscillations following an exponential decay. In contrast, the data reported in Fig. 1(c) clearly show significant deviations from this classical behavior. This observation implies that, in these cases, the viscous force is not a linear function of the tip velocity, precluding the use of the resistive force theory.

Figure 1(d) gives an overview of the crossing time $T$ for the various studied systems. This characteristic time depends mainly on the length and bending modulus of the rod, $B \sim ER^4$, and on the fluid viscosity. Two main tendencies emerge from the graph: the crossing time follows $T \sim L^2$ in the underdamped regime and $T \sim L^3$ in the overdamped one. For the slowest dynamics in the overdamped regime, we even observe a $T \sim L^{3.6}$ regime. However, various types of relaxation can be observed at a given value of the crossing time. Therefore, it is not possible from these raw data to determine *a priori* which law will be followed by a given system. As a matter of fact, all the control parameters are intricately entangled. As shown hereafter, the theoretical model will disentangle this problem.
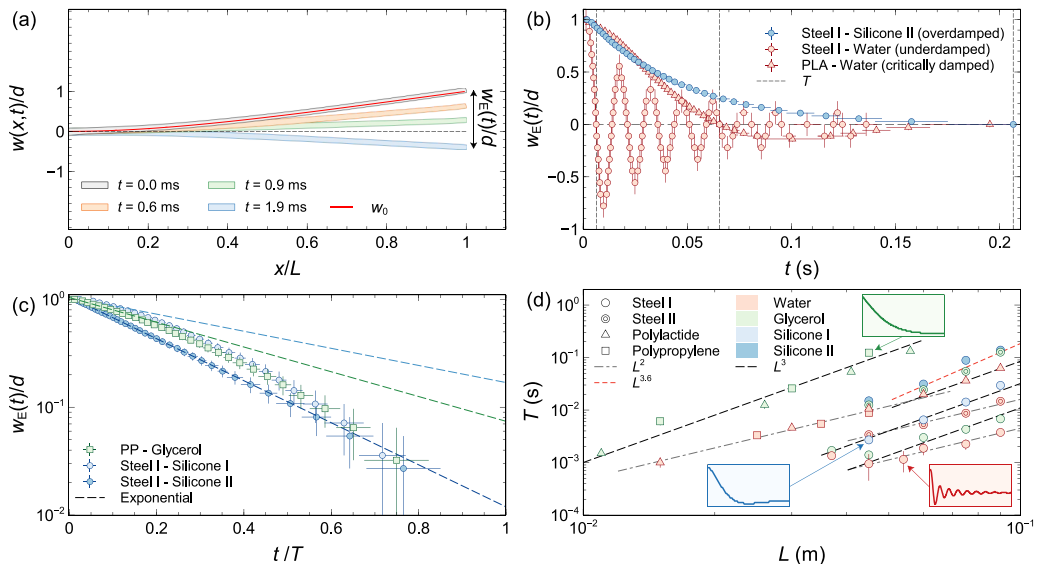
FIG. 1. (a). Snapshots of a deflected stainless steel rod of length $L = 54$ mm oscillating in water at various times as indicated. The horizontal dashed line indicates the equilibrium position of the rod whereas the red solid line represents the initial shape (6). (b), (c) Evolution of the rescaled position of the tip of rod $w_E(t)/d$ as a function of time. (b) Representative temporal variations of $w_E(t)/d$ as the rod materials and the fluid are changed, showing three types of evolution: overdamped, underdamped, and critically damped. $L = 9.0$ cm and $R = 0.4$ mm for the steel rod and $R = 0.2$ mm for PLA rod. The viscosity of the silicone I and II are, respectively, 1.1 and 5.5 Pa s. The crossing times $T$ are also indicated. (c) Representative evolution of $w_E(t)/d$ as a function of the rescaled time $t/T$ in the overdamped regime, showing two types of relaxation dynamics characterized either by a nearly exponential decay or by a polynomial decay: $L = 4.5$ cm and $R = 0.15$ mm for PP and $L = 9.0$ cm and $R = 0.40$ mm for steel. (d) Evolution of the crossing time $T$ as a function of the rod length $L$ for various fluids and rod materials and geometry: 5 GPa $\leqslant E \leqslant$ 165 GPa, 1400 kg/m$^3$ $\leqslant \rho_s \leqslant$ 8300 kg/m$^3$, 0.15 mm $\leqslant R \leqslant$ 0.4 mm, 1.1 cm $\leqslant L \leqslant$ 9.0 cm, $10^{-3}$ Pa s $\leqslant \mu \leqslant$ 10 Pa s and 950 kg/m$^3$ $\leqslant \rho_l \leqslant$ 1100 kg/m$^3$. Insets: representative temporal variations of $w_E(t)/d$.

## III. MODEL

The main objective of the theory proposed here is to describe the full motion of the tip of the rod to obtain the crossing time $T$ and, when there are several oscillations, the damping time $T^\star$ characterizing the temporal decay of the oscillation amplitudes. We note that although $T$ is the relaxation time for overdamped systems, it is related to the oscillation frequency when the system is underdamped, $T^\star$ becoming the true relaxation time. The system is critically damped when $T$ and $T^\star$ have similar values.

### A. Main equation

To describe the experiments reported in Sec. II, we consider a homogeneous cylindrical rod clamped at one extremity ($x = 0$) and free at the other end ($x = L$). Describing the planar motion of the rod is a complex problem requiring to solve the dynamic elastica equation coupled to the Navier-Stokes equations where boundary conditions apply on the moving rod. We propose here to decouple the governing equations by simply adding an effective viscous force to the beam equation which then reads as [66]

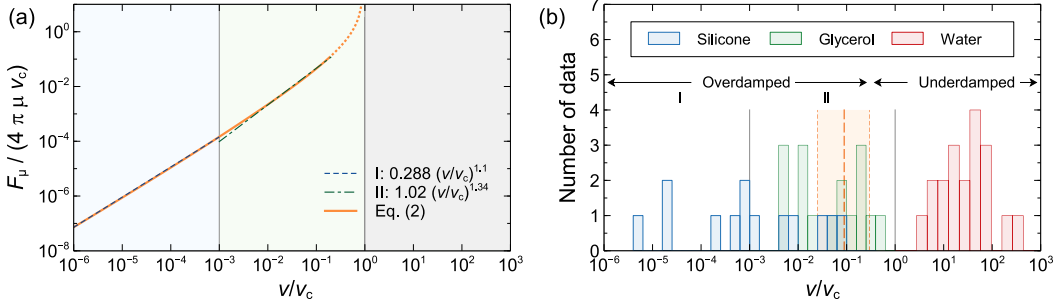$$\bar{\rho}_{sl}\, \partial_t^2 w(x, t) = -B\, \partial_x^4 w(x, t) - F_\mu, \tag{1}$$

FIG. 2. (a) Evolution of the rescaled viscous force $\bar{F}_\mu = F_\mu/(4\pi\mu\,v_c)$, given by Eq. (2), as a function of the rescaled velocity $\bar{v} = v/v_c$ together with two power-law approximations: $\bar{F}_\mu = 1.02\,\bar{v}^{1.34}$ for $\bar{v} \in [1, 200] \times 10^{-3}$ and $\bar{F}_\mu = 0.288\,\bar{v}^{1.1}$ for $\bar{v} < 10^{-3}$. The gray shaded area indicated the region where Eq. (2) is not valid. (b) Number of experimental data for given types of fluids as a function of $v/v_c$ where the velocity is estimated as $v = d/T$. The orange shaded area indicated data for which the experimental profiles $w_E(t)$ have 2 zeros (critically damped regime). Outside this region, the profiles have either 1 zero (overdamped regime) or more than 2 zeros (underdamped regime).

where $w(x, t)$ is the transverse displacement along the vertical axis, $B = EI$ is the bending modulus of the rod where $I$ is the area moment of inertia, and $\bar{\rho}_{sl} = (\rho_s + \rho_l)S \equiv \rho_{sl}S$ is the linear mass density of the rod supplemented by the linear mass of the displaced fluid (hydrodynamic mass [67]), $S$ being the section area of the rod.

The expression of the viscous force per unit length $F_\mu$ is *a priori* complicated since it depends on the local fluid velocity which varies in space and time. Here, we propose to use the viscous drag experienced by a rigid cylinder moving at a constant speed perpendicular to its symmetry axis obtained by solving the Stokes equations with the Oseen's correction [68]:

$$F_\mu = \frac{4\pi\mu\,v}{1/2 - \gamma_E - \ln[v/v_c]}, \quad v_c = \frac{4\mu}{\rho_l\,R}, \tag{2}$$

where $v$ is the (constant) cylinder velocity and $\gamma_E \simeq 0.577$ is the Euler constant. This expression is, by construction, valid when the Reynolds number is small, i.e., Re $\simeq v/v_c \ll 1$, and indeed it diverges when $v/v_c \simeq 0.926$. Higher-order corrections to the expression of the viscous drag exists [69,70] but they will not be considered here.

As shown in Fig. 2(a), the evolution of the rescaled viscous force $F_\mu/(4\pi\mu\,v_c)$ as a function of the rescaled velocity $v/v_c$ can be approximated by two power laws depending on the range of $v/v_c$. Figure 2(b) shows how the experiments are distributed as a function of $v/v_c$ when $v$ is estimated as $d/T$, the nature of damping regime are also indicated. Interestingly, we notice that the overdamped regime is spreading across the transition between the two power-law regions I and II. In the region I where $v/v_c \lesssim 10^{-3}$, the viscous force grows almost linearly with the velocity and the relaxation dynamics should thus be characterized by a nearly exponential decay [Eq. (2) behaves linearly with $v$ when $v/v_c \lesssim 10^{-10}$]. In contrast, in the region II where $10^{-3} \lesssim v/v_c \lesssim 0.2$, the evolution of the viscous force deviates significantly from a linear growth which should impact the relaxation dynamics. Therefore, the viscous force (2) allows already to understand qualitatively the two types of relaxation dynamics observed in the overdamped regime.

Notice that the force (2) deviates significantly from a power law when $v/v_c \gtrsim 0.2$ [see Fig. 2(a)]. Nevertheless, as we will show below, the viscous force is negligible in this regime when computing the crossing time $T$. In addition, after few oscillations, the velocity of the tip of the rod decreases such that the expression (2) becomes valid. Therefore, the damping time $T^\star$ computed with Eq. (2) can be compared to the experimental data provided it is measured experimentally after few oscillations.

We will thus consider the following expression for the nonlinear viscous force:

$$F_\mu = 4\pi \mu \beta v_c^{1-\sigma} v^\sigma, \tag{3}$$

where $\beta = 1.02 \simeq 1.0$ for $\sigma = 1.34 \simeq \frac{4}{3}$ and $\beta = 0.288$ for $\sigma = \frac{11}{10}$ [see Fig. 2(a)].

Combining Eq. (1) with the expression (3) of the viscous force, we obtain the main equation used to describe the experimental data presented in Sec. II B:

$$\bar{\rho}_{sl} \partial_t^2 w = -B \partial_x^4 w - 4\pi \mu \beta v_c^{1-\sigma} S_g |\partial_t w|^\sigma, \tag{4}$$

where $S_g$ is the sign of $\partial_t w$ such that the viscous force is always acting against the rod motion. Since the rod is clamped at one extremity and free at the other end and is released from initial position with a vanishing velocity, Eq. (4) needs to be solved with the following boundary and initial conditions:

$$w(0, t) = \partial_x w(x, t)\big|_{x=0} = 0, \tag{5a}$$

$$\partial_x^2 w(x, t)|_{x=L} = \partial_x^3 w(x, t)\big|_{x=L} = 0, \tag{5b}$$

$$w(x, 0) = w_0(x), \quad \partial_t w(x, t)\big|_{t=0} = 0. \tag{5c}$$

For the shape of the initially bent rod $w_0(x)$, we use the solution of $B \partial_x^4 w_0(x) = q$ given by

$$w_0(\bar{x})/d = \bar{x}^2(\bar{x}^2 - 4\bar{x} + 6)/3, \tag{6}$$

where $\bar{x} = x/L$ and $d = qL^4/(8B)$. Figure 1(a) shows that the expression (6) fits nicely the initial shape of the rod prior to its release.

## B. Crossing time scalings and adimensionalization

When the bending modulus of the rod is large and/or the viscosity of fluid is low, the tip of the rod oscillates around its equilibrium position at a high frequency $\nu \simeq (4T)^{-1}$ [see Fig. 1(b)]. In this underdamped regime, the viscous force can be neglected to compute $T$ from Eq. (4) that becomes, in order of magnitude,

$$\frac{\bar{\rho}_{sl} d}{T^2} \sim \frac{Bd}{L^4} \quad \Rightarrow T \sim 2\Big[\frac{\rho_{sl}}{E}\Big]^{1/2} \frac{L^2}{R}, \tag{7}$$

where we have used $\partial_t^2 w \sim d/T^2$, $\partial_x^4 w \sim d/L^4$, $\bar{\rho}_{sl} = \pi R^2 \rho_{sl}$, and the bending modulus of a cylindrical rod $B = \pi E R^4/4$. The scaling $T \sim L^2$ is in agreement with the experimental data obtained in the underdamped regime [see Fig. 1(d)]. On the contrary, when the bending modulus of the rod is low and/or the viscosity of fluid is large, the motion of the rod is overdamped and there are no oscillations [see Figs. 1(b) and 1(c)]. In this regime, the rod inertia can be neglected and Eq. (4) leads in order of magnitude ($\partial_t w \sim d/T$) to

$$Bd/L^4 \sim 4\pi \mu v_c^{1-\sigma} (d/T)^\sigma. \tag{8}$$

Therefore, we have

$$T \sim 4\Big[\frac{4\mu^2 \rho_l dR}{E^3}\Big]^{1/4} \Big[\frac{L}{R}\Big]^3 \quad \text{for} \quad \sigma = \frac{4}{3}, \tag{9a}$$

$$T \sim 8\Big[\frac{32\mu^9 \rho_l dR}{E^{10}}\Big]^{1/11} \Big[\frac{L}{R}\Big]^{40/11} \quad \text{for} \quad \sigma = \frac{11}{10}. \tag{9b}$$

The two trends observed in Fig. 1(d), namely $T \sim L^3$ or $L^{3.6}$, correspond thus to two different overdamped regimes, their behavior being determined by the value of $v/v_c$.

The transition between the underdamped and overdamped regimes occurs when both values of $T$, given by Eqs. (7) and (9a), are equal. From this equality, we obtain a dimensionless parameter
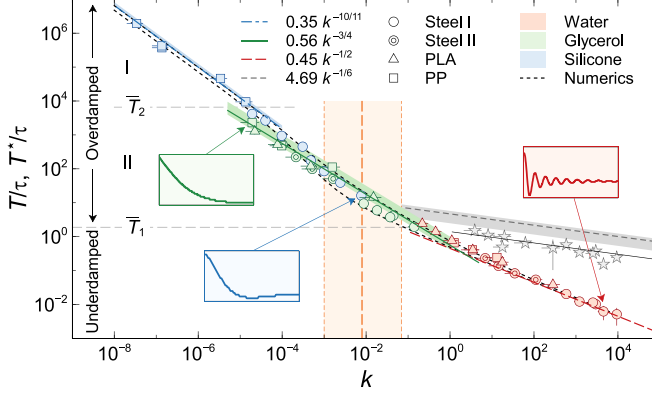
FIG. 3. Evolution of the experimental rescaled crossing time $T/\tau$ as a function of the control parameter $k$, defined by Eq. (10), for various types of rods and fluids. The data for the damping time $T^\star/\tau$ are represented by star symbols. The black solid line represents the theoretical expression (24a) divided by 3. The orange shaded area highlights the critically damped regime as deduced theoretically whereas the horizontal dashed lines show the transition between the three regimes. The blue, green, and gray shaded areas and the dotted black curves show the variations of the theoretical scalings and of the numerical solution of Eqs. (1) and (2) as $\bar{d}$ is varied within its experimental range ($0.4 \leqslant \bar{d} \leqslant 10.5$). Insets: positions of the tip of the rod as a function of time for some representative cases: overdamped, critically damped, and underdamped regimes.

$k/\bar{d}$ merging all the relevant experimental parameters of the system, where

$$k = \frac{E\rho_{sl}R^6}{64\mu^2 L^4}, \quad \bar{d} = \frac{d}{\ell}, \quad \ell = \frac{\rho_{sl}R}{\rho_l}. \tag{10}$$

At the transition between the underdamped and overdamped regimes, we thus have $k/\bar{d} = 1$ by construction. Since $0.4 \lesssim \bar{d} \lesssim 10.5$ in the experiments, $k$ is also close to 1 at this transition (see Fig. 3). The quantity $\ell$ appears thus as a suitable length scale for the transverse motion of the rod and will be used below to rescale $w$. Finally, one natural timescale of this problem $\tau$ is obtained by dividing $\ell$ by $v_c$:

$$\tau = \frac{\rho_{sl}R^2}{4\mu}. \tag{11}$$

Equation (4) can now be adimensionalized using these length scales and timescales:

$$\partial_{\bar{t}}^2 \bar{w}(\bar{x}, \bar{t}) = -k \, \partial_{\bar{x}}^4 \bar{w}(\bar{x}, \bar{t}) - \beta \, S_g |\partial_{\bar{t}} \, \bar{w}(\bar{x}, \bar{t})|^\sigma, \tag{12}$$

where $\bar{w} = w/\ell$, $\bar{x} = x/L$, $\bar{t} = t/\tau$ and $k$, $\ell$, and $\tau$ given by Eqs. (10) and (11). The three regimes identified above, Eqs. (7) and (9), can be written in rescaled variables as follows:

$$\bar{T} \sim k^{-1/2} \quad \text{when} \quad k \gg 1 \quad \text{(underdamped)}, \tag{13a}$$

$$\bar{T} \sim (\bar{d})^{\frac{\sigma-1}{\sigma}} k^{-1/\sigma} \quad \text{when} \quad k \ll 1 \quad \text{(overdamped)}. \tag{13b}$$

The scalings $\bar{T} = \bar{T}(k)$ in the two overdamped regimes involve a coefficient $\bar{d}$ that still depends on the control parameters. Indeed, it is not possible to rescale the variables so that the dynamics of all three regimes will be described by a unique master curve. Nevertheless, in the experiments, the coefficient $(\bar{d})^{\frac{\sigma-1}{\sigma}}$ varies moderately between 0.8 and 1.8 for $\sigma = \frac{4}{3}$ and between 0.9 and 1.2 for $\sigma = \frac{11}{10}$. Therefore, this coefficient will be taken into account through an effective error on the scaling coefficients that will be determined in Sec. IV A.

Figure 3 shows that the rescaled crossing times $T/\tau$ measured for various fluids and rods collapse on a master curve which follows closely the expected scalings (13). The three scalings can be roughly associated to different immersing fluids. The overdamped regimes I and II are related to experiments conducted mainly in silicone oil and glycerol, respectively. The rods immersed in water follow the underdamped regime. In-between these asymptotic regimes, the damping time $T^\star$ characterizing the decay of the amplitude envelope becomes close to the crossing time $T$. This region corresponds to critical damping where the tip of the rod barely oscillates before reaching its equilibrium position. The transitions between the two overdamped regimes and between the overdamped and underdamped regimes occur when $v/v_c \simeq 10^{-3}$ and $v/v_c \simeq 1$, respectively [see Fig. 2(a)]. Using $v = d/T$, these relations in rescaled variables become $\bar{T}_2 \simeq 1000\,\bar{d}$ and $\bar{T}_1 \simeq \bar{d}$, respectively. Since the averaged value of $\bar{d}$ is 6.6 for the overdamped data with $k < 10^{-4}$ and 3.0 for data with $10^{-3} < k < 1$, the transition regions for the crossing time are $\bar{T}_2 \simeq 6.6 \times 10^3$ and $\bar{T}_1 \simeq 3.0$ which agree well with the transition observed in Fig. 3. Notice that, because the transition between the two overdamped regimes is controlled by the value of $v/v_c$ and not by $k$, there exists a small region near $k = 10^{-5}$ where both regimes coexist.

In the next sections, we will study the temporal evolution of the free end of the rod $\bar{w}_E(\bar{t}) = \bar{w}(1, \bar{t})$ obtained from Eq. (12) and compare it to the experimental dynamics. In the process, we will be able to determine the numerical prefactors of the scalings (13) through asymptotic analyses.

## IV. ASYMPTOTIC THEORIES AND COMPARISON WITH EXPERIMENTS

### A. Overdamped regime $k \rightarrow 0$

The scaling (13b) shows that, when $k \ll 1$, the quantity $T/(\tau k^{-1/\sigma})$ is of order 1. Therefore, if we rescale time as $\tilde{t} = t/(\tau k^{-1/\sigma}) = \bar{t}\, k^{1/\sigma}$, Eq. (12) becomes

$$k^{2/\sigma - 1} \partial_{\tilde{t}}^2 \bar{w}(\bar{x}, \tilde{t}) = -\partial_{\bar{x}}^4 \bar{w}(\bar{x}, \tilde{t}) - \beta\, S_g |\partial_{\tilde{t}}\, \bar{w}(\bar{x}, \tilde{t})|^\sigma. \tag{14}$$

This equation contains only quantities of order 1 in contrast with Eq. (12) where $\bar{t}$ is large when $k$ is small. Therefore, the limit $k \rightarrow 0$ can now be considered since all other quantities will remain of order 1. In this limit, the term with the highest temporal derivative disappears. This term cannot rigorously be neglected because, without it, the initial conditions (5c) cannot be all satisfied. In this type of singular perturbation problem [71], the inertial term creates a boundary layer near $\tilde{t} = 0$ whose size decreases when $k$ decreases. The asymptotic expression for small $k$ corresponds thus to the so-called "outer" solution of the problem. Since we are interested in the profile at much larger time, i.e., up to $\tilde{T} = O(1)$, we can consider this asymptotic expression as a good approximation.

In the limit $k \rightarrow 0$, Eq. (14) reduces to

$$\beta[-\partial_{\tilde{t}}\, \bar{w}(\bar{x}, \tilde{t})]^\sigma = \partial_{\bar{x}}^4 \bar{w}(\bar{x}, \tilde{t}). \tag{15}$$

The sign $S_g$ of the velocity appearing in Eq. (14) is removed since there is no oscillation in this regime and $\partial_{\tilde{t}}\, \bar{w} \leqslant 0$. This equation involves only a first-order temporal derivative and must be solved with the boundary and initial conditions (5) without imposing a vanishing initial velocity. Using the separation of variables $\bar{w}(\bar{x}, \tilde{t}) = \bar{w}_E(\tilde{t})\, g(\bar{x})$, the nonlinear partial differential equation (PDE) (15) reduces to two ordinary differential equations (ODEs)

$$\dot{w}_E = -[\eta^4/\beta]^{1/\sigma}\, \bar{w}_E^{1/\sigma}, \quad \bar{w}_E(0) = \bar{d}, \tag{16a}$$

$$g'''' = \eta^4 g^\sigma, \quad g(0) = g'(0) = g''(1) = g'''(1) = 0, \tag{16b}$$

where $\eta^4$ is the separation constant and the overdot and prime indicate time and spatial derivative, respectively. The nonlinear eigenvalue Eq. (16b) can be solved numerically since, at $\tilde{t} = 0$, $\bar{w}(1, 0) = g(1) = 1$. This last condition fixes the value of the separation constant to $\eta_1 \simeq 1.8916 \simeq \frac{70}{37}$ for $\sigma = \frac{11}{10}$ and $\eta_2 \simeq 1.9285 \simeq \frac{27}{14}$ for $\sigma = \frac{4}{3}$. The nonlinear Eq. (16a) is then integrated and
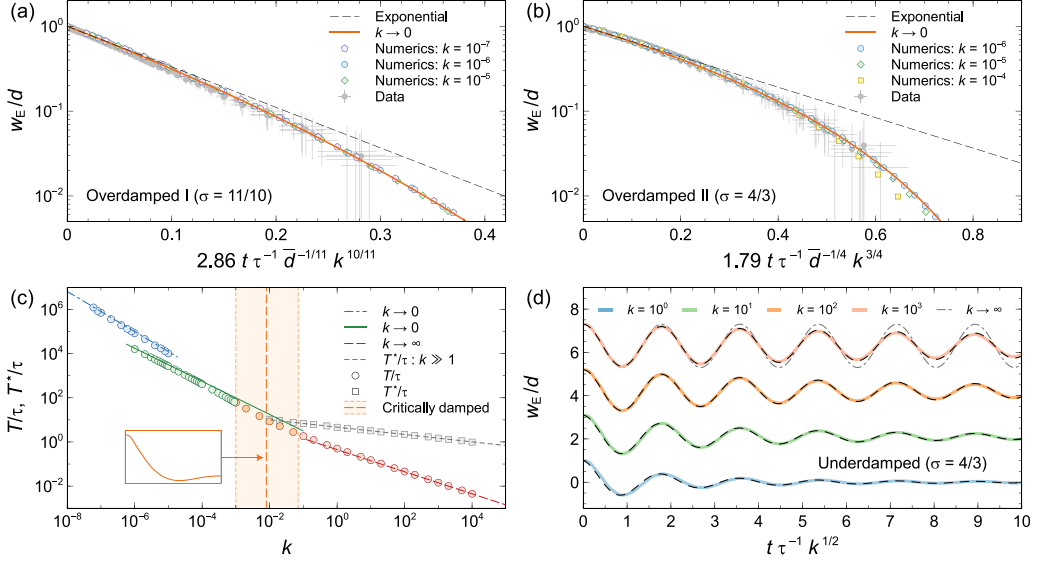
FIG. 4. (a), (b) Evolution of the rescaled position of the tip of the rod $w_E/d$ as a function of a rescaled time for the overdamped regimes I and II. Data obtained by solving numerically Eq. (12) with $\bar{d} = 1$ and $\sigma = \frac{11}{10}$ (a) or $\sigma = \frac{4}{3}$ (b) are compared to the experimental data and the asymptotic theoretical curves (17). (c) Evolution of the crossing and damping times as a function of $k$ extracted from numerical solutions of Eq. (12) with $\bar{d} = 1$ (symbols) together with analytical asymptotic behaviors: Eq. (18a) (dashed-dotted line), Eq. (18b) (solid line), Eq. (23) (dashed line), Eq. (24b) (short-dashed line). The orange shaded area highlights the critically damped regime. Inset: temporal evolution of $w_E/d$ at $k = k_c \simeq 8 \times 10^{-3}$. (d) Comparison between the temporal evolution of $w_E/d$ obtained by solving numerically Eq. (12) with $\sigma = \frac{4}{3}$ and $\bar{d} = 1$ in the underdamped regime (solid curves) and the profiles (24a) obtained from a multiple-scale analysis (dashed curves). The dashed-dotted curve indicates the asymptotic theoretical curve (22) obtained in the undamped regime. The numerical and theoretical data have been shifted vertically for each value of $k$ for clarity.

yields the position of the tip of the rod as a function of time. Returning to the physical variables, we have for each value of $\sigma$

$$\frac{w_E(t)}{d} = \left[ 1 - 2.86 \frac{k^{10/11}}{\bar{d}^{1/11}} \frac{t}{\tau} \right]^{11} \quad \text{(overdamped I)}, \tag{17a}$$

$$\frac{w_E(t)}{d} = \left[ 1 - 1.79 \frac{k^{3/4}}{\bar{d}^{1/4}} \frac{t}{\tau} \right]^{4} \quad \text{(overdamped II)}, \tag{17b}$$

where $k$ and $\tau$ are given by Eqs. (10) and (11). In these overdamped regimes, the relaxation dynamics of the tip of the rod $w_E(t)$ is not characterized by an exponential decay, as predicted by a linear theory, but by a polynomial decay as first suggested by experiments [see Fig. 1(c)]. Figures 4(a) and 4(b) show that, once the time is properly rescaled, the numerical solutions of Eq. (12) at small $k$ and the experimental data in overdamped regimes collapse on the proposed asymptotic curves (17) showing the good quality of these approximations. With these relations, the crossing time corresponding to $w_E = 0$ can be computed and is given by

$$T/\tau \simeq 0.35 \, \bar{d}^{1/11} k^{-10/11} \quad \text{(overdamped I)}, \tag{18a}$$

$$T/\tau \simeq 0.56 \, \bar{d}^{1/4} k^{-3/4} \quad \text{(overdamped II)}, \tag{18b}$$

which agrees well with the crossing times extracted from the numerical solutions of Eq. (12) [see Fig 4(c)].

To compare to the data, $\bar{d}$ is varied between 0.4 and 10.5 as in the experiments. Figure 3 shows that Eqs. (18) describes very well the crossing time measured experimentally in the overdamped regime over almost six and eight orders of magnitude for $T/\tau$ and $k$, respectively.

As the tip of the rod approaches its equilibrium position, its velocity decreases so that, *a priori*, a transition from the overdamped II to the overdamped I regime could happen during a given experiment. Such a transition would occur if $v_E/v_c$ becomes smaller than $\bar{v}^* \simeq 10^{-3}$ where $v_E(t) = dw_E/dt$ is the velocity of the tip of the rod. Using Eq. (17b), we can compute $v_E(t)$ and the time $t^*$ at which $v_E/v_c = \bar{v}^*$. The position of the tip of the rod at $t = t^*$ is found to be $w_E^*/d = (\bar{v}^* \bar{T}/4\bar{d})^{4/3}$. In our experiments performed in the overdamped II regime $w_E^* < 0.6 R$. Therefore, we cannot observe such a transition since it would happen when the tip of the rod is at a distance from its equilibrium smaller than the rod radius.

## B. Undamped regime $k \to \infty$

Before discussing the underdamped regime in the next section where both regular oscillations and decay are observed, we first analyze an idealized case where there is no damping. The scaling (13a) shows that, when $k \gg 1$, the quantity $T/(\tau k^{-1/2})$ is of order 1. Therefore, if we rescale time as $\tilde{t} = t/(\tau k^{-1/2}) = \bar{t} \, k^{1/2}$, Eq. (12) becomes

$$\partial_{\tilde{t}}^2 \bar{w}(\bar{x}, \tilde{t}) = -\partial_{\bar{x}}^4 \bar{w}(\bar{x}, \tilde{t}) - k^{\sigma/2-1} \beta S_g |\partial_{\tilde{t}} \bar{w}(\bar{x}, \tilde{t})|^\sigma. \tag{19}$$

Again, this equation contains only quantities of order 1 in contrast with Eq. (12) where $\bar{t}$ is small when $k$ is large. In the limit $k \to \infty$, Eq. (19) reduces to

$$\partial_{\tilde{t}}^2 \bar{w}(\bar{x}, \tilde{t}) = -\partial_{\bar{x}}^4 \bar{w}(\bar{x}, \tilde{t}). \tag{20}$$

This equation describes the oscillation of a rod in a fluid of negligible viscosity and must be solved with the boundary and initial conditions (5). Using the separation of variables $\bar{w}(\bar{x}, \tilde{t}) = \bar{w}_E(\tilde{t}) \, g(\bar{x})$, this linear PDE reduces to two ODEs

$$\ddot{\bar{w}}_E = -\Sigma^4 \, \bar{w}_E, \quad \bar{w}_E(0) = \bar{d}, \quad \dot{\bar{w}}_E(0) = 0, \tag{21a}$$

$$g'''' = \Sigma^4 \, g, \quad g(0) = g'(0) = g''(1) = g'''(1) = 0, \tag{21b}$$

where $-\Sigma^4$ is the separation constant. The linear eigenvalue Eq. (21b) is easily solved and nontrivial solutions exist provided $1 + \cos(\Sigma) \cosh(\Sigma) = 0$ whose lowest solution is $\Sigma \simeq 1.8751 \simeq \frac{15}{8}$ [16]. We show in Appendix A that considering only the first mode is sufficient for the initial condition (6). The linear Eq. (21a) is then integrated and yields the position of the tip of the rod as a function of time. Returning to the physical variables, it reads as

$$\frac{w_E(t)}{d} = \cos(\omega t), \quad \omega = \frac{\Sigma^2 \, k^{1/2}}{\tau}, \quad \Sigma \simeq \frac{15}{8}. \tag{22}$$

In this undamped regime, there is obviously no attenuation of the oscillation's amplitude.

Figure 4(d) shows that, once the time is properly rescaled, all the numerical solutions of Eq. (12) at large $k$ have the same frequency which is well captured by the asymptotic expression (22) obtained for the ideal undamped regime. Therefore, Eq. (22) can be used to estimate the crossing time $T = 1/(4\nu) = \pi/(2\omega)$, which reads as

$$\frac{T}{\tau} = \frac{\pi}{2\Sigma^2} \, k^{-1/2} \simeq 0.45 \, k^{-1/2}, \tag{23}$$

and agrees well with the crossing times extracted from the numerical solutions of Eq. (12) [see Fig. 4(c)]. Figure 3 shows that Eq. (23) describes very well the crossing time measured experimentally in the underdamped regime over four orders of magnitude for $k$.
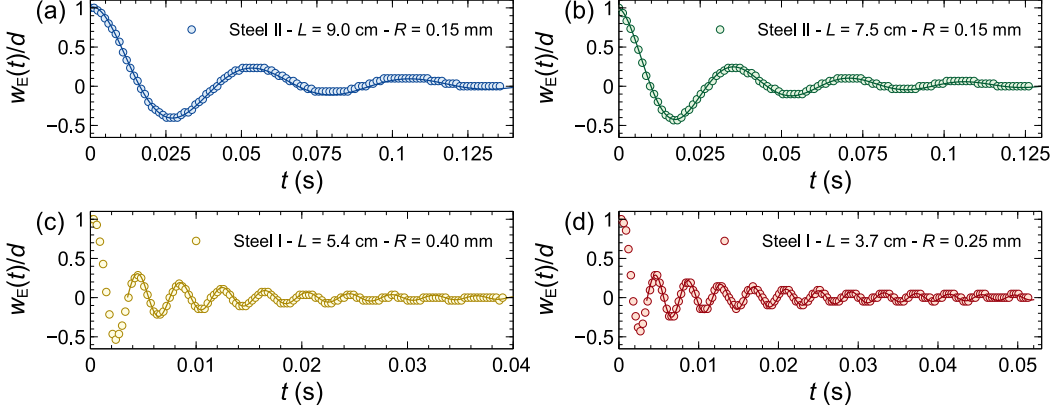
FIG. 5. Representative evolution of $w_E(t)/d$ as a function of time in the underdamped regime where the rod is immersed in water. The solid curves show the theoretical profiles (24a) with $\omega$ and $T^\star$ adjusted for each rod. The values of $T^\star$ obtained are the experimental values reported in Fig. 3 and $\omega$ is computed using Eq. (22) with $k$ and $\tau$ allowed to vary within their experimental errors. The theoretical profiles are limited to time intervals where $v/v_c$ is not too large so that the viscous force (2) is valid.

## C. Underdamped regime $k \gg 1$

The undamped theory presented in the previous section is, of course, unable to describe the temporal decay of the oscillation amplitudes and the related damping time. For this purpose, a multiple-scale analysis is performed (see Appendix A). This approach gives the following temporal evolution of the tip of rod:

$$\frac{w_E(t)}{d} = [1 + t/T^\star]^{-3} \cos(\omega t), \tag{24a}$$

$$\frac{T^\star}{\tau} \simeq 4.69\, \bar{d}^{-1/3} k^{-1/6}, \tag{24b}$$

where the frequency $\omega$ is unchanged compared to the undamped regime and is given by Eq. (22). Figures 4(c) and 4(d) show that Eqs. (24) describe very well the numerical solutions obtained from Eq. (12) for $k \gtrsim 1$ and the related damping time. Figure 3 shows that Eq. (24b) captures very well the evolution with $k$ of the damping time measured experimentally in the underdamped regime. It should be noted, however, that the numerical prefactor is too large by a factor close to 3. Therefore, the amplitude of the oscillations decreases faster experimentally compared to the theoretical prediction but it follows closely the polynomial decay given by Eq. (24a) as shown in Fig. 5. This underestimation is probably due to the fluid flows produced by the rod motion itself. During its periodic oscillations, the rod experiences an additional drag force related to its motion against the flow. Therefore, the rod velocity $\partial_t w$ is no longer equal to the relative velocity between the fluid and the rod when the latter oscillates several times. It is, on average, larger than $\partial_t w$ and the viscous drag is thus probably underestimated in the underdamped regime. A detailed description of the damping time in this regime thus requires to take explicitly the fluid flow into account by solving the Navier-Stokes equation coupled to the beam equation which is beyond the scope of this paper.

## D. Critically damped regime

When the crossing time $T$ and the damping time $T^\star$ are close, the tip of the rod barely oscillates. The interval of $k$ where this critically damped regime takes place can be estimated by equating the expressions of $T$ obtained in the overdamped regime, Eq. (18b), and in the undamped regime, Eq. (23), to the expression (24b) of $T^\star$. This leads to the range $9 \times 10^{-4} \lesssim k \lesssim 7 \times 10^{-2}$ with

TABLE I. Scalings for the rescaled crossing time $T/\tau$, where $\tau$ is defined by Eq. (11), for the three observed regimes and their range of validity with respect to the value of $k$ defined by Eq. (10). $\bar{d}$ is also defined by Eq. (10). The value of $T/\tau$ could also be used to determine the range of validity. Overdamped I: $T/\tau \gtrsim 6000$; overdamped II: $6000 \gtrsim T/\tau \gtrsim 3$; underdamped: $\bar{T} \lesssim 3$.

| Regime | Range $k$ | Scaling |
|---|---|---|
| Overdamped I | $k \lesssim 10^{-5}$ | $T/\tau \simeq 0.35\,\bar{d}^{\frac{1}{11}}\,k^{-\frac{10}{11}}$ |
| Overdamped II | $10^{-5} \lesssim k \lesssim 1$ | $T/\tau \simeq 0.56\,\bar{d}^{\frac{1}{4}}\,k^{-\frac{3}{4}}$ |
| Underdamped | $k \gtrsim 1$ | $T/\tau \simeq 0.45\,k^{-\frac{1}{2}}$ |

a mean value, in logarithmic scale, around $k_c \simeq 8 \times 10^{-3}$. This interval of $k$ is shown in Fig. 4(c) where the inset displays the temporal evolution of $w_E$ at $k = k_c$ which is in-between the overdamped evolution, where the dynamics slowly relaxes to equilibrium, and the underdamped evolution where the system oscillates with a well-defined frequency. This interval of $k$ is also reported in Fig. 3 where the inset shows that the experimental evolution of $w_E$ as a function of time at $k \simeq k_c$ presents the same features than the theoretical profile.

## V. SUMMARY AND DISCUSSIONS

The scalings obtained for the crossing time $T$ and their range of validity are summarized in Table I. In the overdamped I regime, the viscous force (2) can be approximated by a power law without significant impact on the crossing time $T$ [see Fig. 2(a)]. However, in the overdamped II regime, the viscous force departs from a power law and some moderate variation of the scaling reported in Table I can be expected. Actually, the viscous force could have been approximated by $\bar{F}_\mu = 0.79\,\bar{v}^{1.26}$ with the same level of accuracy (see Appendix B). It is easy to repeat the computations performed in Sec. IV A with $\sigma = 1.26 \simeq \frac{5}{4}$. Solving Eq. (16b) leads to $\eta \simeq 1.9156$. Integrating the nonlinear Eq. (16a) yields the temporal evolution of the tip of the rod and a crossing time $T/\tau \simeq 0.52\,\bar{d}^{1/5}\,k^{-4/5}$. Such a small change in the scaling has a negligible impact on the description of the experimental data. Indeed, the ratio between this scaling and the one reported in Table I behaves as $k^{1/20}$ so that it varies by a factor 2 when $k$ varies by a factor $10^5$.

Finally, for a linear viscous force ($v/v_c \lesssim 10^{-10}$, $\sigma = 1$), the usual relaxation time $T \sim \mu L^4/B$ is recovered.

## VI. RELAXATION OF BEES' PAPILLAE

Many bees feed on nectar and collect it by quickly protracting and retracting their tongue (glossa). Surprisingly, the lapping period $T_L \simeq 0.2$ s appears to be essentially independent on the bee species and nectar viscosity $\mu$ (at least on the range [0.001, 0.5] Pa s) [55,56,58,60,62,63,65,72]. The tongue is decorated with hairy papillae, characterized by a length $L \simeq 135$ $\mu$m and a radius $R \simeq 2.1$ $\mu$m for *Bombus terrestris* [63]. When immersed in the nectar, these papillae, which initially adhere to the glossa due to capillary forces, relax to form a brushlike shape within a characteristic relaxation time strongly dependent on the fluid viscosity [63]. When this relaxation time is smaller than the retraction time, i.e., $T < T_R \simeq T_L/2$, the papillae are fully erected before the tongue is retracted out of the nectar. For large viscosity, however, this relaxation time $T$ may become larger than the retraction time $T_R$, an effect inducing a rapid decrease of the capture efficiency. Figure 6(b) shows *in vivo* measurements of the evolution of the ingestion rate of *Bombus*, $Q$, as a function of the sugar concentration $c_s$ [62,63]. At low concentration, $Q$ is essentially constant and decreases significantly when $c_s$ exceed around 50%. Consequently, the energy intake rates first increase with sugar concentration (viscosity) before reaching a maximum around 50% [see Fig. 6(c)]. With the
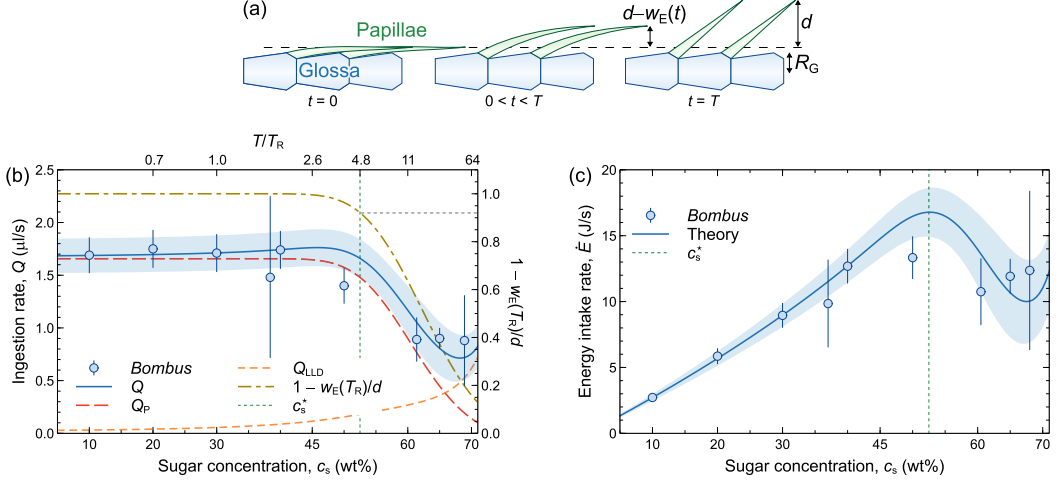
FIG. 6. (a) Schematic of the papillae relaxation dynamics. (b) Comparison between the theoretical ingestion rate $Q$ [see (28)] and *in vivo* measurements for *Bombus* as a function of the sugar concentration together with the contribution $Q_P$ of the papillae and of the dragged film $Q_{LLD}$. The parameter values used are $T_L = (0.20 \pm 0.02)$ s, $E = (1.1 \pm 0.1)$ MPa, $R_G = (95 \pm 5)\,\mu$m, $R = (2.1 \pm 0.1)\,\mu$m, $L = (135 \pm 5)\,\mu$m, $d = L \sin(\pi/4)$, $L_I = 2.0 \pm 0.1$ mm, $\rho_l = (1175 \pm 175)$ kg/m$^3$. (c) Evolution of the energy intake rate $\dot{E}$ as a function of the sugar concentration for several bee species obtained from Eqs. (29) and (28) with the same parameter values. The vertical dotted line indicates the concentration at which $\dot{E}$ is maximum. The symbols represent data obtained by using (29) together with the *in vivo* measurements of $Q$ reported in (b). The shaded areas show the regions spanned by the theoretical curves when the parameters are varied within their error bars.

elastoviscous model proposed here, we can determine the critical viscosity above which the amount of nectar captured per lap starts to decrease.

For this purpose, we first need to determine the nature of the damping regime by estimating $v/v_c \simeq \rho_l dR/(4\mu T)$. A simple inspection of *in vivo* measurements of the papillae relaxation dynamics for a 37% w/w sucrose solution [i.e., $\mu = 5 \times 10^{-3}$ Pa s at 20 °C, see Appendix C] leads to $T > 0.06$ s [63]. Using $d \simeq L \sin(\pi/4) \simeq 95\,\mu$m [63], we obtain $v/v_c < 10^{-4}$. At larger sugar concentrations, $\rho_l/\mu$ is smaller and $T$ is larger so that the ratio $v/v_c$ is smaller than $10^{-4}$. The relaxation dynamics belongs thus to the overdamped I regime.

Using $E \simeq 1.1$ MPa [63] and the values of $R$, $L$, and $d$ given above for *Bombus terrestris* together with the definition of $k$, $\tau$, and $\bar{d}$ given by Eqs. (10) and (11), the evolution of the relaxation time $T$ is obtained as a function of $\mu$ and $\rho_l$ using Eq. (18a):

$$T \simeq 6.12\,\mu^{9/11}\rho_l^{1/11} \simeq 11.64\,\mu^{9/11}, \tag{25}$$

in MKS units. The variation of nectar density can be neglected (see Appendix C). For instance, $\rho_l$ varies between 1000 and 1350 kg/m$^3$ when $\mu$ varies over three orders of magnitude. In addition, $\rho_l$ appears with a very small exponent in Eq. (25), we thus use a constant average value $\rho_l \simeq 1175$ kg/m$^3$. Equation (25) allows to obtain the critical viscosity beyond which the papillae are not fully erected when the tongue retracts out of the nectar, i.e., when $T > T_R$. This happens when $\mu > \mu_c \simeq 0.003$ Pa s corresponding to a 30% w/w sucrose solution at 20 °C (see Appendix C). However, the relaxation dynamics is very slow when the papillae approach their equilibrium position so that they are close to that position at times significantly smaller than $T$. The condition $T > T_R$ leads thus to a crude estimation of critical viscosity beyond which the efficiency of the nectar capture by bees decreases. To obtain a better estimation, it is necessary to incorporate the papillae relaxation dynamics into a nectar capture model.

As proposed in Ref. [63], we assume that the volume of fluid collected by bees is the sum of the volume trapped by their papillae and the volume dragged through a Landau-Levich-Derjaguin (LLD) mechanism [73–76]. The volume of liquid trapped by the papillae when the tongue retracts from the nectar at $t = T_R$ is the volume delimited by the glossa of radius $R_G$ and the tip of the papillae which are at a distance $d - w_E(T_R)$ from the glossa. This volume per unit of time $Q_P$ is thus given by

$$Q_P = \pi \, v_R \left[ \tilde{R}_G^2 - R_G^2 \right], \quad \tilde{R}_G = R_G + d - w_E(T_R), \tag{26}$$

where $w_E(t)$ is given by Eq. (17a) and $v_R = L_I/T_R$ and $L_I$ are the retraction velocity and the immersion length of the tongue, respectively. The thickness $h$ of the film of nectar dragged by the hairy structure through a LLD mechanism during its retraction is given by $h = 1.34 \, \tilde{R}_G \, \mathrm{Ca}^{2/3}$ where $\mathrm{Ca} = \mu v_R / \gamma$ is the capillary number. The surface tension $\gamma \simeq 0.074$ N/m does not vary significantly with the sugar concentration [77]. The volume dragged per unit of time $Q_{\mathrm{LLD}}$ is given by

$$Q_{\mathrm{LLD}} = \pi \, v_R \left[ (\tilde{R}_G + h)^2 - \tilde{R}_G^2 \right]. \tag{27}$$

The total volume of nectar collected per unit of time $Q = Q_P + Q_{\mathrm{LLD}}$ is thus given

$$Q = \pi \, v_R \left[ \tilde{R}_G^2 (1 + 1.34 \, \mathrm{Ca}^{2/3})^2 - R_G^2 \right]. \tag{28}$$

Using the physiological parameters of *Bombus terrestris* [63], Eq. (28) describes well the *in vivo* data reported in Fig. 6(b). For moderate sugar concentrations, the ingestion rate is essentially constant and equal to the volume trapped by the papillae per unit time. The volume of the film dragged through a LLD mechanism is indeed negligible except at very large sugar concentrations $c_s$. The decrease of $Q$ at large $c_s$ is directly related to the papillae relaxation dynamics that induces a decrease of $d - w_E(T_R)$, i.e., the distance between the tip of the papillae and the glossa when the tongue retracts out of the nectar.

Once the ingestion rate is known, the energy intake rate $\dot{E}$ is computed using

$$\dot{E}(c_s) = \sigma \, Q(c_s) \, \rho_l(c_s) \, c_s, \tag{29}$$

where $\sigma = 15.48$ kJ/g is the energy content per unit mass of sugar [65] and $Q$ is given by Eq. (28). The dependence of the nectar mass density on the sugar concentration is here taken into account (see Appendix C) since $\dot{E}$ varies linearly with $\rho_l$ in contrast to $Q$ which depends very weakly on this quantity. Figure 6(c) confirms the good agreement with the model, $\dot{E}$ first grows essentially linearly until it reaches a maximum value at $c_s = c_s^\star \simeq 53\%$ ($\mu_c \simeq 0.02$ Pa s). At this value of the sugar concentration, the papillae are still open at 92% when the tongue retracts out of the nectar and $T \simeq 5 \, T_R$ [see Fig. 6(b)]. For larger sugar concentrations $c_s > c_s^*$, the opening of papillae rapidly decreases as the efficiency of the capture mechanism.

## VII. CONCLUSIONS

The motion of a bent rod immersed in a fluid shows contrasted dynamics according to the experimental conditions (rod material and geometry and the fluid viscosity). When the bending modulus of the rod is large and/or the viscosity is low, the relaxation dynamics is underdamped and the rod oscillates with a well-defined frequency $T^{-1}$ and an amplitude damped with a characteristic time $T^\star$. In contrast, when the bending modulus of the rod is small and/or the viscosity of fluid is large, the relaxation dynamics is overdamped and the rod returns to its equilibrium position in a time $T$ without oscillating [see Fig. 1(b)]. Unexpectedly, the observed motion of the free end of the rod does not follow an exponential decay but a polynomial one [see Fig. 1(c)]. This observation indicates that the viscous force is a nonlinear function of the rod velocity.

The system has been modeled using the dynamical beam equation supplemented by the viscous force experienced by a rigid cylinder moving at a constant speed. This model provides scalings that are used to rescale the experimental data so that they collapse along an essentially unique master

curve as the comparison between Figs. 1(d) and 3 shows. The characteristic times of the dynamics $T$ and $T^{\star}$ are well described by the model as shown in Fig. 3 as well as the temporal evolution of the tip of the rod in all regimes [see Figs. 4(a), 4(b), and 5]. Figure 3 shows, however, that the magnitude of the viscous force is underestimated in the underdamped regime leading to a damping time overestimated by roughly a factor 3. We attribute this effect to the motion of the rod against the flow producing an additional drag force. The model also provides a simple explanation for the existence of two scalings for the relaxation time in the overdamped regime as shown in Fig. 3.

To illustrate the model ability for applications, it has been used in Sec. VI to characterize the overdamped relaxation dynamics of the papillae of the bee tongues observed during nectar feeding. Assuming that the lapping period does not depend significantly on the nectar viscosity, as shown by *in vivo* measurements, the model predicts the evolution of the energy intake rate from the papillae relaxation dynamics which exhibit a maximum of efficiency for sugar concentration around 50%. At larger concentrations (viscosity), the erection of the papillae is further hindered by the viscous drag which impacts the nectar capture and explains the significant drop of the observed ingestion rate.

## APPENDIX A: MULTIPLE-SCALE ANALYSIS

To derive the crossing time $T$ and the damping time $T^{\star}$ in the underdamped regime ($k \gg 1$), we take the nonlinear viscous drag into account as a small perturbation. We first consider the linear unperturbed equation ($k \to \infty$) in Appendix A 1 to obtain an eigenmode expansion and the oscillation frequency. We show that, for our initial condition $\bar{w}(\bar{x}, 0) = \bar{w}_0(\bar{x})$ given by Eq. (6), the first mode provides an excellent approximation of the unperturbed dynamics. We then consider the nonlinear viscous drag as a small perturbation in Appendix A 2 to derive the modulation of the oscillation amplitudes through a multiple-scale analysis.

### 1. Unperturbed equation: Eigenmode expansion

The unperturbed equation is obtained from Eq. (19) in the limit $k \to \infty$:

$$\partial_{\tilde{t}}^2 \bar{w}(\bar{x}, \tilde{t}) = -\partial_{\bar{x}}^4 \bar{w}(\bar{x}, \tilde{t}), \tag{A1}$$

which must be solved with the boundary and initial conditions (5) and (6). Using the separation of variables $\bar{w}(\bar{x}, \tilde{t}) = f(\tilde{t})g(\bar{x})$, we obtain

$$\frac{\ddot{f}(\tilde{t})}{f(\tilde{t})} = -\frac{g''''(\bar{x})}{g(\bar{x})} = -\Sigma^4, \tag{A2}$$

where $-\Sigma^4$ is the separation constant and where the overdot and prime denote temporal and spatial derivatives. We thus obtain two ODEs

$$\ddot{f} = -\Sigma^4 f, \quad f(0) = \bar{d}, \quad \dot{f}(0) = 0, \tag{A3a}$$

$$g'''' = \Sigma^4 g, \quad g(0) = g'(0) = g''(1) = g'''(1) = 0, \tag{A3b}$$

where the boundary and initial conditions are obtained from Eqs. (5) and (6) taking into account the separation of variables.

Equation (A3a) is readily solved and yields

$$f(\tilde{t}) = \bar{d} \, \cos(\Sigma^2 \tilde{t}). \tag{A4}$$

The general solution of Eq. (A3b) reads as

$$g(\bar{x}) = a\,e^{\Sigma\bar{x}} + b\,e^{-\Sigma\bar{x}} + c\,e^{i\Sigma\bar{x}} + d\,e^{-i\Sigma\bar{x}}, \tag{A5}$$

where $a$, $b$, $c$, and $d$ are constants. Using the boundary conditions for $g$, we obtain the following system of four linear equations:

$$\begin{pmatrix} 1 & 1 & 1 & 1 \\ \Sigma & -\Sigma & i\Sigma & -i\Sigma \\ \Sigma^2 e^{\Sigma} & \Sigma^2 e^{-\Sigma} & -\Sigma^2 e^{i\Sigma} & -\Sigma^2 e^{-i\Sigma} \\ \Sigma^3 e^{\Sigma} & -\Sigma^3 e^{-\Sigma} & -i\Sigma^3 e^{i\Sigma} & i\Sigma^3 e^{-i\Sigma} \end{pmatrix} \begin{pmatrix} a \\ b \\ c \\ d \end{pmatrix} = 0. \tag{A6}$$

This system admits nontrivial solutions if and only if the determinant of the coefficient matrix is vanishing which gives the condition

$$1 + \cos(\Sigma)\cosh(\Sigma) = 0. \tag{A7}$$

This Eq. (A7) admits a countably infinite set of eigenvalues:

$$\Sigma = \Sigma_n, \quad n = 0, 1, 2, \dots \tag{A8}$$

where $\Sigma_0 \simeq 1.8751 \simeq 15/8$, $\Sigma_1 \simeq 4.6941$, $\Sigma_2 \simeq 7.8548$, $\Sigma_3 \simeq 10.996$, etc. Notice that we have in good approximation $\Sigma_{n>0} \simeq (2n+1)\pi/2$. Solving the system of Eqs. (A6) and taking into account (A7), the eigenmodes $g_n$, defined up to a multiplicative constant, reads as

$$g_n(\bar{x}) = \cosh(\Sigma_n\bar{x}) - \cos(\Sigma_n\bar{x}) + \alpha[\sin(\Sigma_n\bar{x}) - \sinh(\Sigma_n\bar{x})], \tag{A9}$$

where

$$\alpha = [\cos\Sigma_n + \cosh\Sigma_n]/[\sin\Sigma_n + \sinh\Sigma_n]. \tag{A10}$$

As for standard Sturm-Liouville problems, two eigenmodes associated to two different eigenvalues are orthogonal. It can also be shown that each eigenmode is normalized such that we have

$$\int_0^1 g_n(\bar{x})\,g_m(\bar{x})\,d\bar{x} = \delta_{nm}, \tag{A11}$$

where $\delta_{nm}$ is the Kronecker symbol.

Since Eq. (A1) is linear, its general solution for a vanishing initial velocity and satisfying the boundary conditions can be written as a linear combination of the eigenmodes

$$\bar{w}(\bar{x}, \tilde{t}) = \bar{d} \sum_{n=0}^{\infty} A_n \cos\left(\Sigma_n^2 \tilde{t}\right) g_n(\bar{x}). \tag{A12}$$

The remaining coefficient $A_n$ is determined by the initial condition

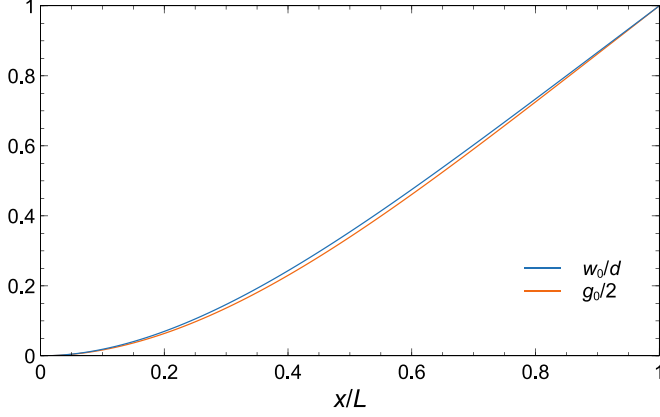$$\bar{w}(\bar{x}, 0) = \bar{w}_0(\bar{x}) = \bar{d} \sum_{n=0}^{\infty} A_n g_n(\bar{x}). \tag{A13}$$

Using the orthogonality relation (A11), we obtain

$$A_n = \bar{d}^{-1} \int_0^1 \bar{w}_0(\bar{x})\,g_n(\bar{x})\,d\bar{x}, \tag{A14}$$

where $A_0 \simeq 0.5067$, $A_1 \simeq 7.15 \times 10^{-3}$, $A_2 \simeq 5.35 \times 10^{-4}$, $A_3 \simeq 9.96 \times 10^{-5}$, etc. Therefore, we have in very good approximation

$$\bar{w}(\bar{x}, \tilde{t}) \simeq \frac{\bar{d}}{2} \cos\left(\Sigma_0^2 \tilde{t}\right) g_0(\bar{x}) \simeq \cos\left(\Sigma_0^2 \tilde{t}\right) \bar{w}_0(\bar{x}) \tag{A15}$$

FIG. 7. Comparison between $\bar{w}_0$ and $g_0/2$.

as shown in Fig. 7. The temporal evolution of the tip of the rod is then given by

$$\bar{w}(1, \tilde{t}) = \bar{w}_E(\tilde{t}) \simeq \bar{d} \, \cos\left(\Sigma_0^2 \tilde{t}\right), \quad \Sigma_0 \simeq \frac{15}{8}, \tag{A16}$$

as reported in the main text since $\tilde{t} = k^{1/2} t / \tau$ [see Eq. (22)].

### 2. Perturbed equation: Multiple-scale analysis

#### a. Differential equations for the eigenmode expansion coefficients

In order to find corrections to the unperturbed solution (A12), we use the following eigenmode expansion:

$$\bar{w}(\bar{x}, \tilde{t}) = \sum_{n=0}^{\infty} A_n \, u_n(\tilde{t}) \, g_n(\bar{x}), \tag{A17}$$

with $u_n(0) = \bar{d}$ and $\dot{u}_n(0) = 0$ and where $g_n$ are the eigenmodes of the unperturbed system given by Eq. (A9). With such an expansion, the boundary conditions are automatically satisfied. In addition, this procedure transforms the nonlinear PDE (19) into an infinite set of ODEs for the coefficients $u_n$ of the eigenmode expansion which can be analyzed by a multiple-scale approach.

Substituting Eq. (A17) into (19) with $\sigma = \frac{4}{3}$, we obtain

$$\sum_{n=0}^{\infty} A_n \, \ddot{u}_n(\tilde{t}) \, g_n(\bar{x}) = -\sum_{n=0}^{\infty} A_n \, u_n(\tilde{t}) \, g_n''''(\bar{x}) - \epsilon S_g \left| \sum_{n=0}^{\infty} A_n \, \dot{u}_n(\tilde{t}) \, g_n(\bar{x}) \right|^{4/3}, \tag{A18}$$

where $S_g$ is the sign of the quantity inside the absolute value and $\epsilon = k^{-1/3} \ll 1$. Using Eq. (A3b), we have

$$\sum_{n=0}^{\infty} A_n \left[ \ddot{u}_n(\tilde{t}) + \Sigma_n^4 u_n(\tilde{t}) \right] g_n(\bar{x}) = -\epsilon h(\bar{x}, \tilde{t}), \tag{A19a}$$

$$h(\bar{x}, \tilde{t}) = S_g \left| \sum_{n=0}^{\infty} A_n \, \dot{u}_n(\tilde{t}) \, g_n(\bar{x}) \right|^{4/3}. \tag{A19b}$$

Since the set of eigenmodes $g_n$ forms a basis, we can write

$$h(\bar{x}, \tilde{t}) = \sum_{n=0}^{\infty} B_n(\tilde{t}) g_n(\bar{x}), \qquad (A20)$$

with

$$B_n(\tilde{t}) = \int_0^1 h(\bar{x}, \tilde{t}) g_n(\bar{x}) d\bar{x}, \qquad (A21)$$

where we used Eq. (A11). Therefore, Eq. (A19a) becomes

$$\sum_{n=0}^{\infty} A_n \left[ \ddot{u}_n(\tilde{t}) + \Sigma_n^4 u_n(\tilde{t}) + \epsilon \frac{B_n(\tilde{t})}{A_n} \right] g_n(\bar{x}) = 0. \qquad (A22)$$

Since this last equation must be valid for all $\bar{x}$, we obtain the infinite set of ODEs to solve for the function $u_n$:

$$\ddot{u}_n(\tilde{t}) + \Sigma_n^4 u_n(\tilde{t}) + \epsilon \frac{B_n(\tilde{t})}{A_n} = 0, \quad n = 0, 1, 2, \ldots \qquad (A23a)$$

$$\text{with} \quad u_n(0) = \bar{d}, \quad \dot{u}_n(0) = 0. \qquad (A23b)$$

As already shown for the unperturbed case ($\epsilon = 0$), the computation is simpler in our case since a single-mode analysis is accurate enough. Indeed, setting $\tilde{t} = 0$ in Eq. (A17) we obtain Eq. (A13) where the coefficients $A_n$ are still given by Eq. (A14). Therefore, in good approximation, we can set $A_0 = \frac{1}{2}$ and $A_{n>0} = 0$ such that Eq. (A17) reduces to

$$\bar{w}(\bar{x}, \tilde{t}) \simeq \tfrac{1}{2} u_0(\tilde{t}) g_0(\bar{x}) \simeq u_0(\tilde{t}) \bar{w}_0(\bar{x})/\bar{d}, \qquad (A24)$$

where $u_0$ is solution of the following ODE:

$$\ddot{u}_0(\tilde{t}) + \Sigma_0^4 u_0(\tilde{t}) + 2\epsilon B_0(\tilde{t}) = 0, \qquad (A25a)$$

$$\text{with} \quad u_0(0) = \bar{d}, \quad \dot{u}_0(0) = 0, \qquad (A25b)$$

and where

$$B_0(\tilde{t}) = \int_0^1 h(\bar{x}, \tilde{t}) g_0(\bar{x}) d\bar{x}, \qquad (A26)$$

with

$$h(\bar{x}, \tilde{t}) = \left[ \frac{g_0(\bar{x})}{2} \right]^{4/3} S_g |\dot{u}_0(\tilde{t})|^{4/3}, \qquad (A27)$$

where $S_g$ is the sign of $\dot{u}_0$ since $g_0$ is positive. Substituting Eq. (A27) into (A26) and using Eq. (A9) with $n = 0$, we obtain

$$2B_0(\tilde{t}) \simeq 0.8942 \, S_g |\dot{u}_0(\tilde{t})|^{4/3} \simeq \frac{76}{85} S_g |\dot{u}_0(\tilde{t})|^{4/3}. \qquad (A28)$$

Therefore, the final form of the ODE to solve is

$$\ddot{u}_0(\tilde{t}) + \Sigma_0^4 u_0(\tilde{t}) + \frac{76\,\epsilon}{85} S_g |\dot{u}_0(\tilde{t})|^{4/3} = 0, \qquad (A29a)$$

$$\text{with} \quad u_0(0) = \bar{d}, \quad \dot{u}_0(0) = 0, \quad \Sigma_0 \simeq \frac{15}{8}. \qquad (A29b)$$

### b. Multiple-scale analysis

We now use a multiple-scale analysis to solve Eq. (A29). Indeed, when $\epsilon = 0$, we already know that the solution is periodic. The nonlinear term modulates the oscillation amplitudes over a much longer timescale which diverges when $\epsilon \to 0$. This allows us to introduce a short timescale $t_s = \tilde{t}$, over which one oscillation takes place, and a long timescale $t_\ell = \epsilon \tilde{t}$, over which the oscillation amplitudes decay, and assume that $u_0$ depends on both timescales considered as independent variables [71]: $u_0 = u_0(t_s, t_\ell; \epsilon)$, where we have written the explicit dependence on the small parameter $\epsilon$. At the first order in $\epsilon$, this implies that

$$\frac{du_0}{d\tilde{t}} = \dot{u}_0 = \partial_{t_s} u_0 + \epsilon \, \partial_{t_\ell} u_0, \tag{A30a}$$

$$\frac{d^2 u_0}{d\tilde{t}^2} = \ddot{u}_0 = \partial_{t_s}^2 u_0 + 2\epsilon \, \partial_{t_s, t_\ell}^2 u_0. \tag{A30b}$$

In addition, we consider the following expansion:

$$u_0(t_s, t_\ell; \epsilon) = u_0^{(0)}(t_s, t_\ell) + \epsilon \, u_0^{(1)}(t_s, t_\ell). \tag{A31}$$

Substituting Eqs. (A30) and (A31) into Eq. (A29), we obtain the following PDE:

$$\partial_{t_s}^2 u_0^{(0)} + \Sigma_0^4 u_0^{(0)} + \epsilon \left[ \partial_{t_s}^2 u_0^{(1)} + \Sigma_0^4 u_0^{(1)} + 2\partial_{t_s, t_\ell}^2 u_0^{(0)} + \frac{76}{85} S_g \left| \partial_{t_s} u_0^{(0)} \right|^{4/3} \right] = 0, \tag{A32}$$

together with the initial conditions

$$u_0^{(0)}(0, 0) = \bar{d}, \quad \partial_{t_s} u_0^{(0)}(0, 0) = 0, \tag{A33a}$$

$$u_0^{(1)}(0, 0) = 0, \quad \partial_{t_s} u_0^{(1)}(0, 0) + \partial_{t_\ell} u_0^{(0)}(0, 0) = 0. \tag{A33b}$$

*Order $\epsilon^0$.* At the leading order, Eq. (A32) gives

$$\partial_{t_s}^2 u_0^{(0)} + \Sigma_0^4 u_0^{(0)} = 0. \tag{A34}$$

The solution can be written as

$$u_0^{(0)}(t_s, t_\ell) = R(t_\ell) \cos \left[ \Sigma_0^2 t_s + \theta(t_\ell) \right], \tag{A35}$$

with the following initial conditions for $R$ and $\theta$ obtained from Eq. (A33a):

$$R(0) = \bar{d} \quad \text{and} \quad \theta(0) = 0. \tag{A36}$$

*Order $\epsilon^1$.* At the next order, Eq. (A32) gives

$$\partial_{t_s}^2 u_0^{(1)} + \Sigma_0^4 u_0^{(1)} = -2\partial_{t_s, t_\ell}^2 u_0^{(0)} - \frac{76}{85} S_g \left| \partial_{t_s} u_0^{(0)} \right|^{4/3}$$

$$\equiv G(t_s, t_\ell). \tag{A37}$$

The inhomogeneous term on the right-hand side of Eq. (A37) contains resonant terms producing secular contributions in the solution for $u_0^{(1)}$ whose envelope grows as $t_s$. Therefore, because of these resonant terms, the expansion (A31) is valid only for $\epsilon t_s \sim t_\ell \ll 1$. In order to obtain an expansion valid at least up to the long timescale, those resonant terms must be canceled by a suitable choice of $R$ and $\theta$. The resonant terms are easy to identify since they are solutions of the homogeneous Eq. (A37). The right-hand side of Eq. (A37) reads as

$$G = 2\Sigma_0^2 \dot{R} \sin(X) + 2\Sigma_0^2 R \dot{\theta} \cos(X) - \frac{76}{85} \Sigma_0^{8/3} R^{4/3} S_g |-\sin(X)|^{4/3}, \tag{A38}$$

$$\text{with} \quad X = \Sigma_0^2 t_s + \theta(t_\ell), \tag{A39}$$

where $S_g$ is the sign of $-\sin(X)$. The last term can be developed in Fourier series which leads to

$$G = 2\Sigma_0^2 \dot{R} \sin(X) + 2\Sigma_0^2 R \dot{\theta} \cos(X) - \frac{76}{85}\Sigma_0^{8/3} R^{4/3} [-b_1 \sin(X) + b_3 \sin(3X) + \cdots], \quad \text{(A40)}$$

with

$$b_1 = \frac{48\,\Gamma\left(\frac{2}{3}\right)}{7\sqrt{\pi}\,\Gamma\left(\frac{1}{6}\right)}, \quad b_3 = \sqrt{\frac{\pi}{3}}\frac{16}{91\,\Gamma\left(\frac{1}{3}\right)\Gamma\left(\frac{7}{6}\right)}. \quad \text{(A41)}$$

The resonant terms are those proportional to $\sin(X)$ and $\cos(X)$. Requiring that they vanish yields the following ODEs for the amplitude $R$ and the phase $\theta$:

$$\dot{R} + \frac{38\,b_1}{85}\Sigma_0^{2/3} R^{4/3} = 0, \quad R(0) = \bar{d}, \quad \text{(A42)}$$

$$\dot{\theta} = 0, \quad \theta(0) = 0. \quad \text{(A43)}$$

Solving these equations leads to

$$R(t_\ell) = \bar{d}\left[1 + \frac{38\,b_1 \Sigma_0^{2/3} \bar{d}^{\,1/3}}{255}t_\ell\right]^{-3}, \quad \theta(t_\ell) = 0. \quad \text{(A44)}$$

Using $t_\ell = \epsilon\,\tilde{t} = k^{-1/3}\tilde{t} = k^{1/6}t/\tau$, we obtain

$$R(t) = \bar{d}\left[1 + \frac{t}{T^\star}\right]^{-3}, \quad \theta(t) = 0, \quad \text{(A45a)}$$

$$\frac{T^\star}{\tau} = \frac{255}{38\,b_1 \Sigma_0^{2/3} \bar{d}^{\,1/3}}k^{-1/6} \simeq \frac{4.69}{\bar{d}^{\,1/3}}k^{-1/6}. \quad \text{(A45b)}$$

Combining Eq. (A24) with (A35) and (A45a) and $t_s = \tilde{t} = k^{1/2}t/\tau$, we obtain the approximate spatiotemporal evolution of the rod

$$\bar{w}(\bar{x}, t) \simeq \frac{\cos(\omega t)}{[1 + t/T^\star]^3}\,\bar{w}_0(\bar{x}), \quad \omega = \frac{\Sigma_0^2 k^{1/2}}{\tau}, \quad \text{(A46)}$$

with $\Sigma_0 \simeq \frac{15}{8}$ and $\bar{w}_0$ given by Eq. (6). The motion of the tip of the rod is thus given by

$$\bar{w}_E(t) \simeq \bar{d}\,[1 + t/T^\star]^{-3}\cos(\omega t), \quad \text{(A47)}$$

with $T^\star$ given by Eq. (A45b) as reported in the main text [see Eq. (24a)].

## APPENDIX B: POWER-LAW APPROXIMATION OF THE VISCOUS FORCE

In the region $10^{-6} \leqslant v/v_c \leqslant 10^{-3}$, the viscous force (2) behaves in very good approximation as a power law [see Fig. 2(a)]. In the region $10^{-3} \leqslant v/v_c \leqslant 0.2$, where most of our experiments in the overdamped II regime take place, the viscous force (2) does not behave precisely as a power law and some variation of the exponent can be expected depending on the way the fit is performed.

To determine the exponent of the power law in the overdamped II regime, we take $N = 10^3$ points $(\ln(\bar{v}_i), \ln[\bar{F}_\mu(\bar{v}_i)])$ for $\bar{v}_i$ in the range $[\bar{v}_i, \bar{v}_N] = [10^{-3}, 0.2]$ and we perform a linear regression.

If $\bar{v}_i$ varies by a constant step, i.e., $\bar{v}_i = \bar{v}_1 + (i - 1)\Delta$, where $\Delta = (\bar{v}_N - \bar{v}_1)/(N - 1)$ and $i = 1, \ldots, N$, the exponent obtained from the regression is 1.34. In the paper we use $\frac{4}{3}$ for simplicity.

If $\ln(\bar{v}_i)$ varies by a constant step, i.e., $\ln(\bar{v}_i) = \ln(\bar{v}_1) + (i - 1)\Delta$, where $\Delta = [\ln(\bar{v}_N) - \ln(\bar{v}_1)]/(N - 1)$ and $i = 1, \ldots, N$, the exponent obtained from the regression is $1.26 \simeq 5/4$ (see Fig. 8).

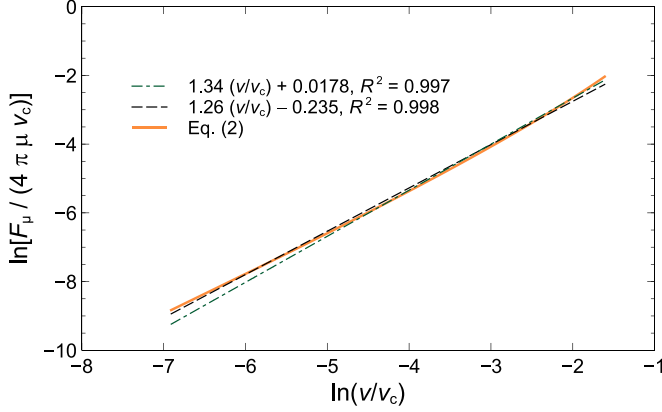The regressions have been performed with *Mathematica* using the "LinearModelFit" command.

FIG. 8. Evolution of the rescaled viscous force $\bar{F}_\mu = F_\mu/(4\pi\mu v_c)$, given by Eq. (2), as a function of the rescaled velocity $\bar{v} = v/v_c$, together with two power-law approximations in the overdamped II regime. The coefficient of determination $R^2$ is similar for both power laws.

## APPENDIX C: SUGAR SOLUTION VISCOSITY AND DENSITY

Figure 9(a) shows the evolution of the viscosity of various sugar solutions as a function of the sugar concentration at $20\,°C$ [78]. The data are nicely fitted using the following expression adapted from Ref. [79]:

$$\mu_{20°}(x) = (976.27)^{-1}\, 10^{0.9652\,x/(1-x)} 10^{0.8572\,x^2}, \tag{C1}$$

where $x \in [0, 1]$ is the sucrose concentration. The numerical coefficients have been determined using the sucrose data but slight modifications allow to fit the other types of sugar. The viscosity changes slightly with the temperature and at $30\,°C$, we have [79]

$$\mu_{30°}(x) = (1097)^{-1}\, 10^{0.8752\,x/(1-x)} 10^{1.01\,x^2}. \tag{C2}$$

Figure 9(b) shows the evolution of the density of various sugar solutions as a function of their viscosity [78]. The data are also nicely fitted using the following expression:

$$\rho_l = 1134\left[\ln\left(\frac{\mu + 0.00132}{0.00175}\right)\right]^{1/10}, \tag{C3}$$
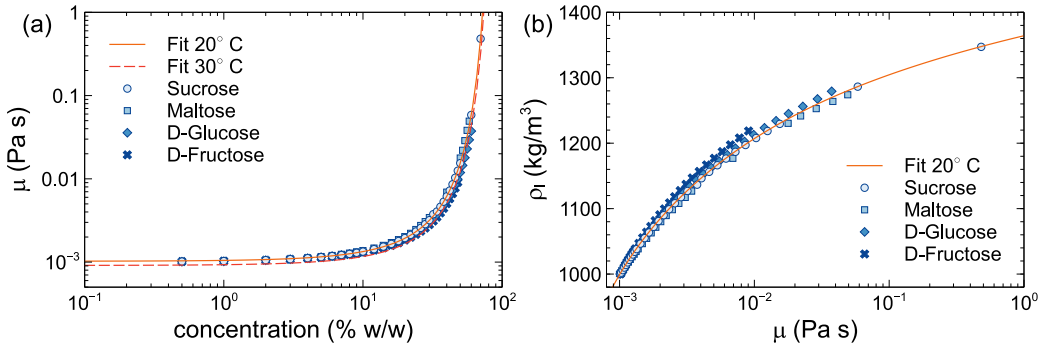


FIG. 9. (a) Viscosity of sugar solutions as a function of the sugar concentration at $20\,°C$ [78] together with the fit (C1). The fit at $30\,°C$ is shown for comparison. (b) Density of sugar solutions as a function of the viscosity [78].

where $\mu$ is measured in Pa s. Again, the numerical coefficients have been determined using the sucrose data but slight modifications allow to fit the other types of sugar.

---

[1] G. Binnig, C. F. Quate, and Ch. Gerber, Atomic Force Microscope, Phys. Rev. Lett. **56**, 930 (1986).

[2] F. J. Giessibl, Advances in atomic force microscopy, Rev. Mod. Phys. **75**, 949 (2003).

[3] R. Berger, E. Delamarche, H. P. Lang, C. Gerber, J. K. Gimzewski, E. Meyer, and H.-J. Güntherodt, Surface stress in the self-assembly of alkanethiols on gold, Science **276**, 2021 (1997).

[4] R. Bashir, J. Z. Hilt, O. Elibol, A. Gupta, and N. A. Peppas, Micromechanical cantilever as an ultrasensitive pH microsensor, Appl. Phys. Lett. **81**, 3091 (2002).

[5] M. Sepaniak, P. Datskos, N. Lavrik, and C. Tipple, Microcantilever transducers: A new approach in sensor technology, Anal. Chem. **74**, 568A (2002).

[6] L. A. Pinnaduwage, A. Gehl, D. L. Hedden, G. Muralidharan, T. Thundat, R. T. Lareau, T. Sulchek, L. Manning, B. Rogers, M. Jones, and J. D. Adams, A microsensor for trinitrotoluene vapour, Nature (London) **425**, 474 (2003).

[7] J. Chaste, A. Eichler, J. Moser, G. Ceballos, R. Rurali, and A. Bachtold, A nanomechanical mass sensor with yoctogram resolution, Nat. Nanotechnol. **7**, 301 (2012).

[8] J. R. Barnes, R. J. Stephenson, M. E. Welland, C. Gerber, and J. K. Gimzewski, Photothermal spectroscopy with femtojoule sensitivity based on micromechanics, Nature (London) **372**, 79 (1994).

[9] J. Fritz, M. K. Baller, H. P. Lang, H. Rothuizen, P. Vettiger, E. Meyer, H.-J. Güntherodt, C. Gerber, and J. K. Gimzewski, Translating biomolecular recognition into nanomechanics, Science **288**, 316 (2000).

[10] G. Wu, R. H. Datar, K. M. Hansen, T. Thundat, R. J. Cote, and A. Majumdar, Bioassay of prostate-specific antigen (PSA) using microcantilevers, Nat. Biotechnol. **19**, 856 (2001).

[11] R. McKendry, J. Zhang, Y. Arntz, T. Strunz, M. Hegner, H.-P. Lang, M. K. Baller, U. Certa, E. Meyer, H.-J. Güntherodt, and C. Gerber, Multiple label-free biodetection and quantitative DNA-binding assays on a nanomechanical cantilever array, Proc. Natl. Acad. Sci. USA **99**, 9783 (2002).

[12] T. Vo-Dinh, *Nanotechnology in Biology and Medicine: Methods, Devices, and Applications* (CRC Press, Boca Raton, FL, 2017).

[13] S. B. Patil, R. M. Al-Jehani, H. Etayash, V. Turbe, K. Jiang, J. Bailey, W. Al-Akkad, R. Soudy, K. Kaur, R. A. McKendry, T. Thundat, and J. W. Ndieyira, Modified cantilever arrays improve sensitivity and reproducibility of nanomechanical sensing in living cells, Commun. Biol. **1**, 175 (2018).

[14] W. Y. Shih, X. P. Li, H. M. Gu, W. H. Shih, and I. A. Aksay, Simultaneous liquid viscosity and density determination with piezoelectric unimorph cantilevers, J. Appl. Phys. **89**, 1497 (2001).

[15] H. P. Lang, M. Hegner, and Ch. Gerber, Nanomechanical cantilever array sensors, in *Springer Handbook of Nanotechnology*, edited by B. Bhushan (Springer, Berlin, 2017).

[16] J. E. Sader, Frequency response of cantilever beams immersed in viscous fluids with applications to the atomic force microscope, J. Appl. Phys. **84**, 64 (1998).

[17] C. P. Green and J. E. Sader, Torsional frequency response of cantilever beams immersed in viscous fluids with applications to the atomic force microscope, J. Appl. Phys. **92**, 6262 (2002).

[18] S. Basak and A. Raman, Hydrodynamic loading of microcantilevers vibrating in viscous fluids, J. Appl. Phys. **99**, 114906 (2006).

[19] C. A. Van Eysden and J. E. Sader, Frequency response of cantilever beams immersed in viscous fluids with applications to the atomic force microscope: Arbitrary mode order, J. Appl. Phys. **101**, 044908 (2007).

[20] D. R. Brumley, M. Willcox, and J. E. Sader, Oscillation of cylinders of rectangular cross section immersed in fluid, Phys. Fluids **22**, 052001 (2010).

[21] C. A. van Eysden and J. E. Sader, in *Frequency Response of Cantilever Beams Immersed in Viscous Fluids*, in *Resonant MEMS: Fundamentals, Implementation and Application*, edited by O. Brand, I. Dufour, S. M. Heinrich, F. Josse (Wiley, Weinheim, 2015), Chap. 2, pp. 29–53.

[22] J. W. M. Chon, P. Mulvaney, and J. E. Sader, Experimental validation of theoretical models for the frequency response of atomic force microscope cantilever beams immersed in fluids, J. Appl. Phys. **87**, 3978 (2000).

[23] G. I. Taylor, Analysis of the swimming of microscopic organisms, Proc. R. Soc. London A **209**, 447 (1951).

[24] G. I. Taylor, The action of waving cylindrical tails in propelling microscopic organisms, Proc. R. Soc. London A **211**, 225 (1952).

[25] G. J. Hancock, The self propulsion of microscopic organisms through liquids, Proc. R. Soc. London A **217**, 96 (1953).

[26] J. Gray and G. J. Hancock, The propulsion of sea-urchin spermatozoa, J. Exp. Biol. **32**, 802 (1955).

[27] J. E. Drummond, Propulsion by oscillating sheets and tubes in a viscous fluid, J. Fluid Mech. **25**, 787 (1966).

[28] J. Lighthill, Flagellar hydrodynamics, SIAM Rev. **18**, 161 (1976).

[29] E. Lauga and T. R. Powers, The hydrodynamics of swimming microorganisms, Rep. Prog. Phys. **72**, 096601 (2009).

[30] E. Lauga and C. Eloy, Shape of optimal active flagella, J. Fluid Mech. **730**, R1 (2013).

[31] C. W. Wolgemuth, T. R. Powers, and R. E. Goldstein, Twirling and Whirling: Viscous Dynamics of Rotating Elastic Filaments, Phys. Rev. Lett. **84**, 1623 (2000).

[32] M. Manghi, X. Schlagberger, and R. R. Netz, Propulsion with a Rotating Elastic Nanorod, Phys. Rev. Lett. **96**, 068101 (2006).

[33] B. Qian, T. R. Powers, and K. S. Breuer, Shape Transition and Propulsive Force of an Elastic Rod Rotating in a Viscous Fluid, Phys. Rev. Lett. **100**, 078101 (2008).

[34] N. Coq, O. du Roure, J. Marthelot, D. Bartolo, and M. Fermigier, Rotational dynamics of a soft filament: Wrapping transition and propulsive forces, Phys. Fluids **20**, 051703 (2008).

[35] R. Vogel and H. Stark, Motor-driven bacterial flagella and buckling instabilities, Eur. Phys. J. E **35**, 15 (2012).

[36] B. Rodenborn, C.-H. Chen, H. L. Swinneya, Bin Liu, and H. P. Zhang, Propulsion of microorganisms by a helical flagellum, Proc. Natl. Acad. Sci. USA **110**, E338 (2013).

[37] M. K. Jawed, N. K. Khouri, F. Da, E. Grinspun, and P. M. Reis, Propulsion and Instability of a Flexible Helical Rod Rotating in a Viscous Fluid, Phys. Rev. Lett. **115**, 168101 (2015).

[38] M. K. Jawed and P. M. Reis, Deformation of a soft helical filament in an axial flow at low Reynolds number, Soft Matter **12**, 1898 (2016).

[39] M. K. Jawed and P. M. Reis, Dynamics of a flexible helical filament rotating in a viscous fluid near a rigid boundary, Phys. Rev. Fluids **2**, 034101 (2017).

[40] Y. Park, Y. Kim, and S. Lim, Locomotion of a single-flagellated bacterium, J. Fluid Mech. **859**, 586 (2019).

[41] R. E. Johnson, An improved slender-body theory for stokes flow, J. Fluid Mech. **99**, 411 (1980).

[42] R. Cortez, L. Fauci, and A. Medovikov, The method of regularized Stokeslets in three dimensions: Analysis, validation, and application to helical swimming, Phys. Fluids **17**, 031504 (2005).

[43] S. G. Prasath, J. Marthelot, R. Govindarajan, and N. Menon, Relaxation of a highly deformed elastic filament at a fluid interface, Phys. Rev. Fluids **1**, 033903 (2016).

[44] D. J. Howell and N. Hodgkin, Feeding adaptations in the hairs and tongues of nectar-feeding bats, J. Morphol. **148**, 329 (1976).

[45] Y. Winter and O. Von Helversen, Operational tongue length in phyllostomid nectar-feeding bats, J. Mammal. **84**, 886 (2003).

[46] N. Muchhala, Nectar bat stows huge tongue in its rib cage, Nature (London) **444**, 701 (2006).

[47] C. J. Harper, S. M. Swartz, and E. L. Brainerd, Specialized bat tongue is a hemodynamic nectar mop, Proc. Natl. Acad. Sci. USA **110**, 8852 (2013).

[48] A. Rico-Guevara and M. A. Rubega, The hummingbird tongue is a fluid trap, not a capillary tube, Proc. Natl. Acad. Sci. USA **108**, 9356 (2011).

[49] W. Kim, F. Peaudecerf, M. W. Baldwin, and J. W. M. Bush, The hummingbird's tongue: A selfassembling capillary syphon, Proc. R. Soc. B **279**, 4990 (2012).

[50] W. Kim and J. W. M. Bush, Natural drinking strategies, J. Fluid Mech. **705**, 7 (2012).

[51] B. Roman and J. Bico, Elasto-capillarity: Deforming an elastic structure with a liquid droplet, J. Phys.: Condens. Matter **22**, 493101 (2010).

[52] J. Bico, E. Reyssat, and B. Roman, Elastocapillarity: When surface tension deforms elastic solids, Annu. Rev. Fluid Mech. **50**, 629 (2018).

[53] H. Yang, J. Wu, and S. Yan, Effects of erectable glossal hairs on a honeybee's nectar-drinking strategy, Appl. Phys. Lett. **104**, 263701 (2014).

[54] C. Zhao, J. Wu, and S. Yan, Erection mechanism of glossal hairs during honeybee feeding, J. Theor. Biol. **386**, 62 (2015).

[55] C. Zhao, J. Wu, and S. Yan, Observations and temporal model of a honeybee's hairy tongue in microfluid transport, J. Appl. Phys. **118**, 194701 (2015).

[56] J. Chen, J. Wu, and S. Yan, Switchable wettability of the honeybee's tongue surface regulated by erectable glossal hairs, J. Insect Sci. **15**, 164 (2015).

[57] J. Wu, R. Zhu, S. Yan, and Y. Yang, Erection pattern and section-wise wettability of honeybee glossal hairs in nectar feeding, J. Exp. Biol. **218**, 664 (2015).

[58] C.-C. Li, J.-N. Wu, Y.-Q. Yang, R.-G. Zhu, and S.-Z. Yan, Drag reduction effects facilitated by microridges inside the mouthparts of honeybee workers and drones, J. Theor. Biol. **389**, 1 (2016).

[59] Y. Zhao, J. Wu, and S. Yan, The morphology and reciprocation movement of honeybee's hairy tongue for nectar uptake, J. Bionic Eng. **13**, 98 (2016).

[60] R. Zhu, H. Lv, T. Liu, Y. Yang, J. Wu, and S. Yan, Feeding kinematics and nectar intake of the honey bee tongue, J. Insect Behav. **29**, 325 (2016).

[61] Y. Yang, J. Wu, R. Zhu, C. Li, and S. Yan, The honeybee's protrusible glossa is a compliant mechanism, J. Bionic Eng. **14**, 607 (2017).

[62] A. Lechantre, D. Michez, and P. Damman, Collection of nectar by bumblebees: How the physics of fluid demonstrates the prominent role of the tongue's morphology, Soft Matter **15**, 6392 (2019).

[63] A. Lechantre, A. Draux, H.-A. B. Hua, D. Michez, P. Damman, and F. Brau, Essential role of papillae flexibility in nectar capture by bees, Proc. Natl. Acad. Sci. USA **118**, e2025513118 (2021).

[64] D. W. Roubik and S. L. Buchmann, Nectar selection by Melipona and Apis mellifera (Hymenoptera: Apidae) and the ecology of nectar intake by bee colonies in a tropical forest, Oecologia **61**, 1 (1984).

[65] L. D. Harder, Effects of nectar concentration and flower depth on flower handling efficiency of bumble bees, Oecologia **69**, 309 (1986).

[66] L. D. Landau and E. M. Lifshitz, *Theory of Elasticity* (Pergamon, New-York, 1986).

[67] F. M. White, *Fluid Mechanics* (McGraw-Hill, New-York, 2011), p. 579.

[68] H. Lamb, On the uniform motion of a sphere through a viscous fluid, Lond. Edinb. Dubl. Philos. Mag. **21**, 112 (1911).

[69] I. Proudman and J. R. A. Pearson, Expansions at small Reynolds numbers for the flow past a sphere and a circular cylinder, J. Fluid Mech. **2**, 237 (1957).

[70] S. Kaplun, Low Reynolds number flow past a circular cylinder, J. Math. Mech. **6**, 595 (1957).

[71] M. H. Holmes, *Introduction to Perturbation Methods* (Springer, New York, 2013).

[72] L. Shi, S. W. Nicolson, Y. Yang, J. Wu, S. Yan, and Z. Wu, Drinking made easier: Honey bee tongues dip faster into warmer and/or less viscous artificial nectar, J. Exp. Biol. **223**, jeb229799 (2020).

[73] L. Landau and B. Levich, Dragging of a Liquid by a Moving Plate, Acta Physicochim. URSS **17**, 42 (1942).

[74] B. V. Derjaguin, On the thickness of the liquid film adhering to the walls of a vessel after emptying, Acta Physicochim. URSS **20**, 349 (1943).

[75] B. V. Derjaguin and S. M. Levi, *Film Coating Theory* (The Focal Press, London, 1964).

[76] D. Quéré, Fluid coating on a fiber, Annu. Rev. Fluid Mech. **31**, 347 (1999).

[77] V. Aroulmoji, V. Aguié-Béghin, M. Mathlouthi, and R. Douillard, Effect of sucrose on the properties of caffeine adsorption layers at the air/solution interface, J. Colloid Interface Sci. **276**, 269 (2004).

[78] *CRC Handbook of Chemistry and Physics 90th Edition (Internet Version 2010)*, edited by D. R. Lide (CRC Press, Boca Raton, FL, 2010), Chap. 8.

[79] K. A. Pivnick and J. N. McNeil, Effects of nectar concentration on butterfly feeding: Measured feeding rates for Thymelicus lineola (Lepidoptera: Hesperiidae) and a general feeding model for adult Lepidoptera, Oecologia **66**, 226 (1985).